Visible-light-driven BiOI and GO/BiOI photocatalysts for organic pollutants degradation and hydrogen production using low power sources

Socorro Oros-Ruiz[1,2], Hiram Joazet Ojeda-Galván[3,4],
Mildred Quintana[3,4], Roberto Leyva-Ramos[5],
Adriana Isabel Moral-Rodríguez[4,5] and
Esmeralda Mendoza-Mendoza[2,4,5]*

[1]Departamento de Química, Universidad Autónoma Metropolitana-Iztapalapa, Mexico City, Mexico,
[2]Investigadoras e Investigadores por México-CONAHCYT, Ciudad de México, Mexico, [3]Facultad de
Ciencias, Universidad Autónoma de San Luis Potosí, San Luis Potosí, Mexico, [4]Microscopia de Alta
Resolución, Centro de Investigación en Ciencias de la Salud y Biomedicina (CICSAB), Universidad
Autónoma de San Luis Potosí, San Luis Potosí, Mexico, [5]Centro de Investigación y Estudios de Posgrado,
Facultad de Ciencias Químicas, Universidad Autónoma de San Luis Potosí, San Luis Potosí, Mexico

BiOI and (3 wt%)GO/BiOI visible-light-driven photocatalysts were obtained by a
one-pot solvothermal method and successfully applied to the degradation of
single and binary dye solutions of rhodamine B (RhB) and methylene blue (MB)
and H_2 production using very low-power sources. The GO/BiOI with hierarchical
flower morphologies exhibited the highest activity, achieving RhB and MB
photodegradation percentages (%X_{dye}) of 100% and 80%, respectively, in
240 min employing a simple 19 W white LED array. Furthermore, GO/BiOI
dosage and RhB initial concentration play an essential role in dye degradation,
and scavenger assays confirmed that holes and superoxides are the main species
causing RhB oxidation. TOC analysis determined an efficiency of 70%, and after
three uses, the GO/BiOI attained a %X_{RhB} of 84%. The H_2 evolution was performed
under 2 W UV light, yielding 323.25 μmol/h·g of H_2 for BiOI, and the addition of
GO nanosheets increased the photoactivity of GO/BiOI up to 63% (509.61 μmol/
h·g). The catalytic activity of GO/BiOI is superior to values reported in the
literature considering nominal power consumption (kWh) vs. efficiency of RhB
degradation or H_2 production.

KEYWORDS

bismuth compounds, green synthesis, photocatalysis, white LED, water splitting

1 Introduction

Semiconductor photocatalysis is one of the most promising technologies for
addressing global environmental pollution and energy needs. Heterogeneous
photocatalysis can efficiently oxidize various organic pollutants, photoreduce
heavy metals to less toxic oxidation states, produce hydrogen via water splitting,
convert carbon dioxide to fuels, inactivate microorganisms, among others. (Abdullah
et al., 2017; Ke et al., 2017; Quiroz-Cardoso et al., 2019; Segovia-Sandoval et al., 2023;
Gómez-Narváez et al., 2024). Photocatalysis can use simulated visible light or sunlight

to activate semiconductors and, in some cases, achieve the complete mineralization (H_2O and CO_2) of toxic organic molecules, making it a sustainable and environmentally friendly technology.

The use of photocatalysis to treat polluted water and produce clean energy stands out among the many applications of this technology. Organic pollutants commonly detected in water systems include dyes, pharmaceuticals, surfactants, pesticides, personal care products, and aromatic hydrocarbons (Saxena et al., 2020). Dyes present high water solubility, chemical stability, and very low biodegradability; their half-life times under sunlight irradiation are superior to 2000 h (Porter, 1973). Besides, synthetic pigments, such as rhodamine B (RhB), can affect the central nervous system, brain, kidney, and liver in exposed humans. In addition, RhB impedes photosynthesis, and concentrations around 1 mg/L produce colored water, hindering light penetration and disturbing aquatic life (Yusuf et al., 2022).

On the other hand, water splitting into H_2 and O_2 employing semiconductors is recognized as a practical strategy to promote the transition to sustainable and renewable energy sources to alleviate the global energy and environmental crises. Nowadays, H_2 is primarily produced from fossil fuels, including water-gas shift and steam reforming technologies. Clean hydrogen fuel is essential for green energy, as well as biological and environmental processes.

Bismuth oxyhalide (BiOX, X = Cl, I, Br, and F) semiconductors have attracted significant research attention due to their outstanding physicochemical properties. BiOX nanocomposites belong to the V-VI-VII group of ternary oxide semiconductors with the molecular formula expressed as $[M_2O_2]$ $[X_m]$, where M and X are metal and halide elements, respectively. The crystal array consists of fluorite-like $[M_2O_2]$ layers between double halogen $[X_m]$ sheets, forming a layered structure (Bannister, 1935). Among the BiOX family, bismuth oxyiodides, such as BiOI, have been reported as excellent p-type semiconductors for photocatalytic applications. In the electronic structure of BiOI, the O 2p and I 5p states mainly contribute to the valence band maximum (VBM), while the Bi 6p states govern the conduction band minimum (CBM) (Zhao et al., 2012), resulting in a small band gap varying from 1.6 to 2.1 eV (Hou et al., 2019; Wang et al., 2019), and the capability of acting as a visible light-driven photocatalyst. Nevertheless, the use of bare BiOI is limited due to the high recombination rate of photogenerated electron-hole (e^--h^+) pairs. Several approaches have been carried out to increase the lifetime of e^--h^+ pairs in BiOI, such as morphology control during synthesis, surface modification with metals, noble metals, and non-metallic nanoparticles (NPs) or carbonaceous materials, as well as coupling with other semiconductors to design Z-scheme heterojunctions. The latter have shown advanced spatial charge carrier separation and high redox capability at the interface (Li et al., 2019; Yang et al., 2019; Zhang et al., 2019; Xia et al., 2020; Hassani et al., 2021). Among these strategies, graphene oxide (GO) in low contents has been used to decorate the surface of BiOI, which tunes the energy band potential and increases the visible and infrared absorption, producing highly efficient photocatalytic nanocomposites. GO acts as an electron shell that allows the flow of e^- from BiOI to GO, diminishing the e^--h^+ recombination (Moral-Rodríguez et al., 2022).

Several direct and green methodologies, such as hydrothermal, solvothermal, and sonochemical, have been employed to obtain bare and BiOI-based nanocomposites, producing different two- (2D) and three- (3D) dimensional morphologies like micro- and nanoplates, microspheres, hollow microspheres, nanosheets, and others (Yang et al., 2018; Arumugam and Choi, 2020).

Numerous studies have been reported on synthesizing carbonaceous materials/BiOI nanocomposites and BiOI-based heterojunctions and their application to RhB photodegradation. Xia et al. (2020) prepared hierarchical microspheres of (1.5 wt.%)GO/BiOI by a one-step route using polyvinylpyrrolidone (PVP) as a shape-directing reagent. The GO/BiOI nanocomposite attained 35% RhB degradation in 80 min for an initial RhB concentration of 5 mg/L under 125 W Hg lamp irradiation. Hou et al. (2019) designed BiOI decorated with N-doped cattail-based carbon (NCC) via an in-situ self-template quick crystallization mechanism using HCl and acidic acid as solvents to obtain well-defined micro/nano BiOI microspheres. RhB degradation of 92% was achieved using the NCC/BiOI under a 500 W Xe lamp. Zhong et al. (2019) synthesized (3 wt.%)GO/BiOI through precipitation, yielding microspheres of BiOI supported on GO flocculent structures. The activity of GO/BiOI towards RhB photodegradation was 95% within 90 min, employing a 300 W Xe lamp. Hou et al. (2017) obtained nanocomposites of BiOI with activated carbon (AC) by a solvothermal method. The (3.3 wt.%)AC/BiOI compound showed thick sheet-like particles of BiOI loaded onto AC layers, and removed 95% of RhB in 120 min under irradiation of 500 W Xe source. Li et al. (2019) fabricated a BiOBr/BiOI heterojunction (3:1 M ratio) using a direct solvothermal method, that exhibited flower-like microspheres. This heterojunction obtained 100% RhB oxidation after 80 min of irradiation with a 500 W Xe lamp. Liu et al. (2016) reported the preparation of graphene-analogue boron nitride (BN)/BiOI heterojunction following a one-step solvothermal procedure. The (0.5 wt.%)BN/BiOI displayed microsphere shapes of BiOI decorated with smooth layers of BN, and its performance toward RhB photodegradation achieved 93% in 100 min under illumination with a 350 W Xe source.

Regarding the H_2 production over BiOI-containing heterostructures, Shan et al. (2024) synthesized BiOI/β-Bi_2O_3 heterojunction utilizing an electrophoretic deposition method to obtain highly crystalline sheet-like shapes. The (0.12 wt.%)BiOI/β-Bi_2O_3 exhibited high stability and activity, yielding an H_2 evolution rate of 91 μmol/h g under 300 W Xe lamp irradiation. Zhou et al. (2021) prepared CdS microparticles decorated with Bi^0 and BiOI nanosheets by precipitation and solvothermal methods. The Bi^0/BiOI(010)CdS catalyst showed superior performance, achieving an H_2 producing rate of 36,000 μmol/h g using a 300 W Xe lamp. Yang et al. (2021) obtained a well-defined 3D flower-like mesoporous K-BiOI catalyst via the solvothermal method with an S_{BET} area of 26 m^2/g. The H_2 evolution rate recorded for the K-BiOI catalyst was 6,510 μmol/h g under a 300 W Xe light source. Li et al. (2021) constructed a heterojunction by combining BiOI with a Zr-based mesoporous MOF, NU-1000, with a high S_{BET} area of around 1900 m^2/g. Li et al. The (7 wt.%)BiOI/Zr-MOF heterojunction produced 610 μmol/h g of H_2 under a 100 W visible (Vis) LED lamp. Chang et al. (2019) prepared plate-like morphologies of G/AgI/BiOI through solvothermal method. The BiOI containing 10 wt.% of G and Ag showed the highest H_2 production, reaching 183 μmol/h g under a 300 W Hg irradiation. Luévano-Hipólito et al. (2023) fabricated BiOI films via a one-pot microwave

hydrothermal process using mica as a substrate. The films showed well-dispersed micrometric BiOI particles with flower-like shapes due to mica acting as an effective substrate to control the growth of BiOI. The films annealed at 150 °C obtained an H_2 producing rate of 1800 μmol/h g using a 20 W Vis LED lamp.

In this research, highly efficient visible-light-driven photocatalysts of BiOI and GO/BiOI were successfully designed. The hierarchical flower-shaped porous morphologies of BiOI were obtained by a straightforward and green solvothermal method. A low dose of GO was loaded as support for BiOI, which acted as an electron shell to diminish the recombination of photogenerated electron-hole pairs during photocatalysis. The as-prepared BiOI-based photocatalysts were characterized by several techniques to associate the outstanding physicochemical properties with their superior photocatalytic performance exhibited under very low-power irradiation sources. These nanocomposites exhibited a higher performance toward dye degradation and H_2 production than similar ones reported in the literature, by comparing the photocatalytic efficiency vs. the power consumption of the whole process. In addition, the effects of catalyst dosage and initial concentration of RhB on the catalytic activity of the GO/BiOI nanocomposite were analyzed. Scavenger tests were used to determine the main oxidative species producing RhB degradation, and reuse assays were conducted. The performance of GO/BiOI towards the photodegradation of a mixed solution of dyes (RhB and methylene blue, MB) was also investigated.

2 Experimental details

2.1 Synthesis and characterization

The precursor reagents were $Bi(NO_3)_3 \cdot 5H_2O$, KI, and ethylene glycol (E.G.,) supplied by Merck. Solution A was prepared by dissolving 3 mmol of $Bi(NO_3)_3$ in, E.G., (60 mL) and solution B containing 3 mmol of KI in, E.G., (20 mL); both solutions were stirred at 650 rpm for 15 min. Then, solution B was added slowly to solution A to yield solution C, which was magnetically stirred at 650 rpm for 30 min. Solution C was placed in a Teflon-lined stainless-steel autoclave and subjected to a heat treatment at 120 °C for 12 h. The resulting suspension was then centrifuged at 11,000 rpm for 15 min to separate the particles from the reaction media, and the particles were repeatedly washed with ethanol and deionized (DI) water. Finally, the as-prepared BiOI nanoparticles were dried at 60°C for 12 h. As for the GO/BiOI catalyst, the GO (3 wt.%) was added to the, E.G., before incorporating $Bi(NO_3)_3$ into solution A, and then the same procedure as described above was followed. GO was synthesized by a modified Hummers' method (Santamaría-Juárez et al., 2019).

XRD analysis of the BiOI-based photocatalysts were conducted in a Bruker D8 Advance diffractometer operating at 35 kV, 25 mA and using CuK_α radiation (λ = 1.5406 Å). XRD patterns were recorded from 5° to 80° (2θ) at a scanning rate of 0.03°/s. The crystallite size (CS) was determined using the Halder-Wagner method included in the PDXL2 program, Rigaku. Raman studies were performed in a Horiba Xplora Plus spectrometer employing a 532 nm laser and a wavelength interval from 50 to 1700 cm^{-1}. An ISR 2600 Plus integration sphere (220–1,400 nm) attached to a

Shimadzu 2600 UV–Vis spectrophotometer was used for obtaining UV–Vis diffuse absorbance and reflectance spectra. The textural properties of the catalysts were evaluated from the N_2 adsorption-desorption isotherms, determined in a N_2 physisorption analyzer, Micromeritics, model ASAP 2020. The surface area (S_{BET}) was assessed by applying the method proposed by Brunauer, Emmett, and Teller (BET) (Brunauer et al., 1938). The pore size distribution and the total accumulated pore volume were estimated using the Barret-Joyner-Halenda (BJH) method (Barrett et al., 1951). The volume and average diameter of the pores (V_P and D_P) were computed using the procedures recommended by Rouquerol et al. (2014). TEM examinations were carried out in a JEOL JEM-2100 microscope operated at 200 kV, whereas EDS analysis was performed in STEM mode. The point of zero charge (pH_{PZC}) of the as-prepared catalysts was determined by the pH drift method (Mousavi et al., 2016; Si et al., 2020). In brief, 25 mL of 0.01 N NaCl solution at 25°C were poured into 50 mL centrifuge tubes, and the initial pH of the solutions were adjusted in the range between 3 and 11 by adding drops of NaOH and HCl solutions (0.01, 0.1, and 1 N). The initial pH was registered, and 75 mg of catalyst was added to each solution. The solution and catalyst were shaken twice daily for 2 days. Then, the final pH was determined and graphed vs. the initial pH, and the pH_{PZC} was pH at which this plot crossed the line of equality (final pH = initial pH). Photoluminescence (PL) spectra were acquired in an Agilent Cary Eclipse fluorescence spectrophotometer using 334 nm as excitation wavelength.

2.2 Procedure for obtaining adsorption equilibrium and RhB photodegradation rate data

Solutions of known initial concentration of RhB (10–35 mg/L) were prepared; 100 mL of the solution and 100 mg of photocatalyst were brought into contact in a 250 mL glass reactor. The pH of these suspensions was adjusted to 7 with drops of NaOH and HCl solutions (0.01 and 0.1 N), and magnetically stirred at 500 rpm. After 30 min of stirring, an aliquot (1.5 mL) was taken and centrifuged at 4,500 rpm to separate the particles, and the RhB concentration was measured at a wavelength of 554 nm in a Shimadzu 1900 UV-Vis spectrophotometer. Then, the uptake adsorbed of RhB was calculated by performing a mass balance of RhB represented by Eq. 1:

$$q = \frac{V(C_0 - C_e)}{m} \qquad (1)$$

where C_0 and C_e are the initial and equilibrium concentrations of RhB, mg/L; V is the RhB solution volume, L; m is the mass of the photocatalyst, g; q is the mass adsorbed of RhB, mg/g.

RhB photodegradation tests were performed in a 250 mL glass reactor using a white LED array comprised of 78 SMD 5050 LED (16,000 lux, 19 W total electric power) wrapped around the reactor at a 0.5 cm distance. 100 mg of the photocatalyst was contacted with 100 mL of RhB solution (30 mg/L) and sonicated for a few minutes to suspend the particles. After stirring for 30 min in the dark, the LED source was turned on, and the suspension was sampled (1.5 mL) every 30 min; the total volume sampled was less than 10% of the initial

volume. During stirring in the dark, the pH of the suspension was maintained at 7, while the temperature was kept constant at 25 °C throughout the process. Experiments were carried out in duplicate.

The photocatalytic performance of GO/BiOI was investigated by varying the catalyst dosage (catalyst mass/RhB solution volume) from 25/100 to 100/100 mg/mL and RhB initial concentration from 25 to 35 mg/L. For conducting scavenger assays, the following substances were added to the reactor suspension: EDTA disodium salt dihydrate (EDTA-Na$_2$, 0.2 mM), isopropyl alcohol (IPA, 0.2 mM), p-benzoquinone (p-BQ, 0.2 mM), and silver nitrate (AgNO$_3$, 0.2 mM). These substances were used for trapping hydroxyl radicals ($^{\bullet}OH$), holes (h^+), superoxides ($O_2^{\bullet-}$), and electrons (e^-), correspondingly. TOC determination at the beginning and the end of the RhB degradation using GO/BOI was performed in a TOC-L Shimadzu analyzer. In addition, mixtures of RhB + MB (1:1 and 1:2 M ratio) were prepared to study the performance of GO/BiOI in binary dye solutions.

2.3 Photocatalytic hydrogen production evaluation

The hydrogen production was conducted in a homemade quartz reactor of 200 mL, sealed, and containing a 50% V/V methanol-water solution. In this solution, 25 mg of photocatalyst was suspended by stirring. In the center of the reactor was a quartz tube containing a low-intensity Pen Ray mercury lamp (λ = 254 nm, 2 W power consumption, I = 2.2 mW/cm^2). The hydrogen production cycles of the reaction were evaluated for 5 h; samples were taken every 1 h and analyzed using a gas chromatograph, Shimadzu GC-8, coupled to a thermal conductivity detector (TCD) with a 5 Å molecular sieve column.

3 Results and discussion

Figure 1A shows the XRD patterns of BiOI and GO/BiOI, and the diffraction peaks of BiOI (PDF 10–0445) with tetragonal symmetry were detected in the photocatalysts. The Miller indices of the main crystalline planes are indicated in brackets. The crystallographic planes of GO/BiOI appear with lower intensity and slightly shifted to lower 2θ (°) than BiOI due to the expansion of the unit cell of BiOI caused by the interaction between BiOI and GO. For BiOI and GO/BiOI, the CS was determined to be 5.6 and 3.6 nm, respectively.

Figure 1B depicts the Raman spectra of BiOI and GO/BiOI catalysts. The B$_{1g}$ vibrational mode around 84 cm^{-1} is assigned to the Bi-I external stretching bond, whereas the A$_{1g}$ and, E$_g$ about 102 and 149 cm^{-1} are associated with the Bi-I internal stretching bond (Putri et al., 2019). The as-prepared GO showed the D and G characteristic modes around 1,336 and 1,578 cm^{-1}, respectively. The D band is related to disorders at graphene edges and sp^3 defects, while G refers to vibrational stretching of the sp^2 carbon atom. Besides, D and G modes in GO/BiOI are shifted toward lower (red shift) and higher (blue shift) wavenumbers around 1,324 and 1,596 cm^{-1}, correspondingly, due to surface strain changes by contacting GO and BiOI (How et al., 2014).

Figure 2A depicts the N$_2$ adsorption-desorption isotherms on BiOI and GO/BiOI. The N$_2$ isotherms are of type IIb, characteristic of aggregates of platy particles, and the hysteresis loop is H3, typical of mesoporous materials (Rouquerol et al., 2014).

The S$_{BET}$, D$_p$, and V$_p$ of BiOI were 38 m^2/g, 19 nm, and 0.18 cm^3/g, respectively. In the case of GO/BiOI, the S$_{BET}$, D$_p$, and V$_p$ were 46 m^2/g, 12 nm, and 0.14 cm^3/g, respectively, which is consistent with the broader hysteresis loop of the N$_2$ isotherm, indicating smaller pores. Adding GO (3 wt.%) efficiently increases the S$_{BET}$ of GO/BiOI 1.2 times compared to BiOI.
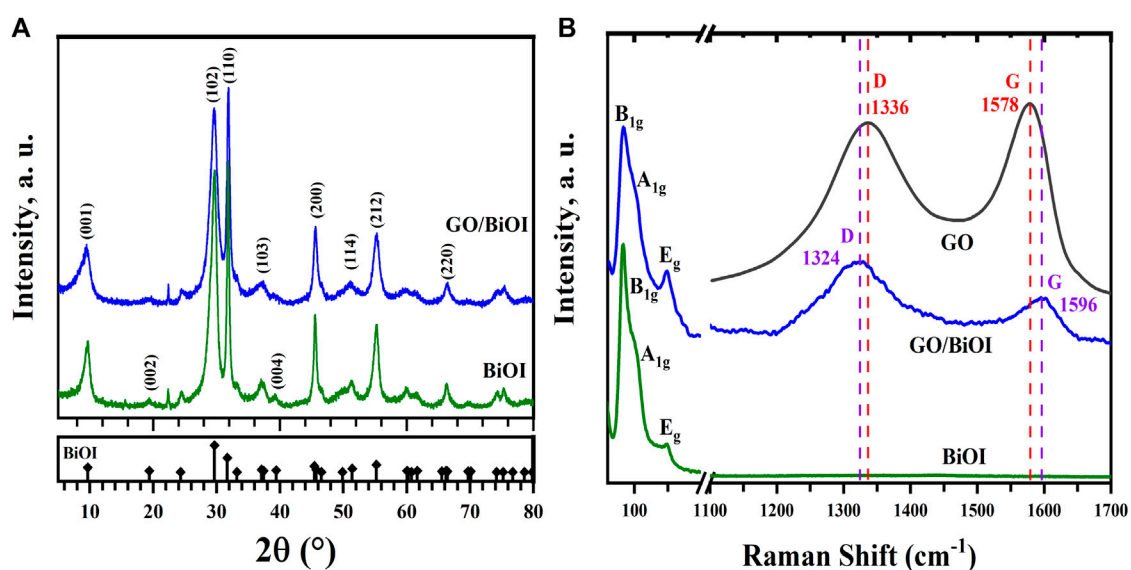
FIGURE 1
(A) XRD patterns, and **(B)** Raman spectra of BiOI and GO/BiOI. The Raman spectrum of GO and the Raman shift of the D and G bands in GO/BiOI are also shown in **(B)**.
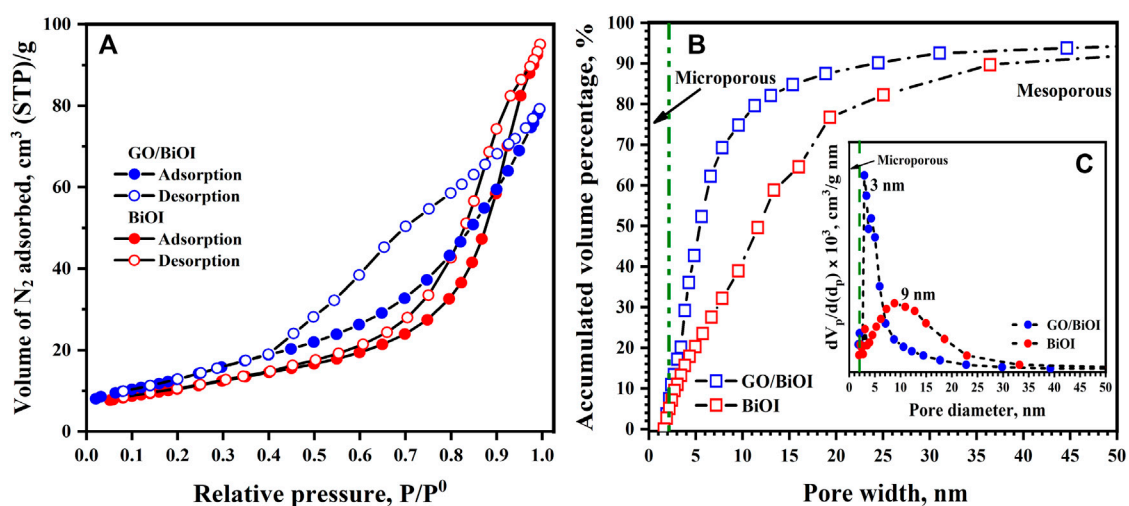
FIGURE 2
(A) N2 adsorption-desorption isotherms on BiOI and GO/BiOI at 77 K, **(B)** the cumulative pore volume, and **(C)** pore size distribution of BiOI and GO/BiOI.

TABLE 1 Crystallite size (CS), Energy gap (E_g), BET area (S_{BET}), pore diameter (D_p), and pore volume (V_p) obtained for the as-prepared photocatalysts.

Sample	CS (nm)	Optical absorption edge (nm)	E_g (eV)	S_{BET} (m²/g)	D_p (nm)	V_p (cm³/g)	pH$_{PZC}$
BiOI	5.6	630	2.07	38	19	0.18	5.40
GO/BiOI	3.6	650	1.96	46	12	0.14	5.13
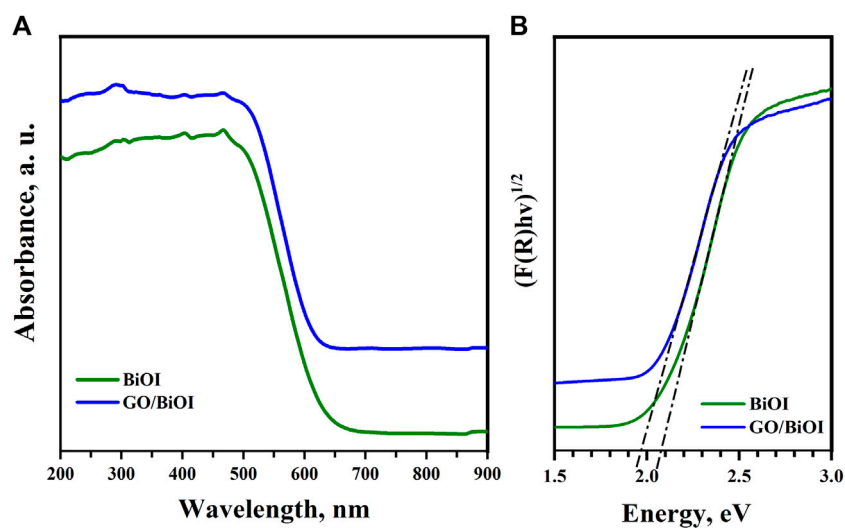
FIGURE 3
(A) UV-Vis DRS absorption spectra, and **(B)** the estimated E_g of the as-prepared catalysts.

The textural properties of the as-prepared catalysts are given in Table 1.

The cumulative total pore volume and pore size distribution of BiOI and GO/BiOI are shown in Figures 2B, C. As can be seen in Figure 2B, both BiOI and GO/BiOI consist mainly of mesopores (2 nm < pore size <50 nm). The pore size distribution reveals that GO/BiOI predominantly contains mesopores with a diameter of 3 nm, while BiOI has mesopores with a diameter of 9 nm, as indicated in Figure 2C. In addition, BiOI showed a broader pore size distribution than GO/BiOI.

Figure 3A exhibits the UV-Vis absorption spectra of BiOI and GO/BiOI, and the catalysts showed UV-Vis photoresponse. The
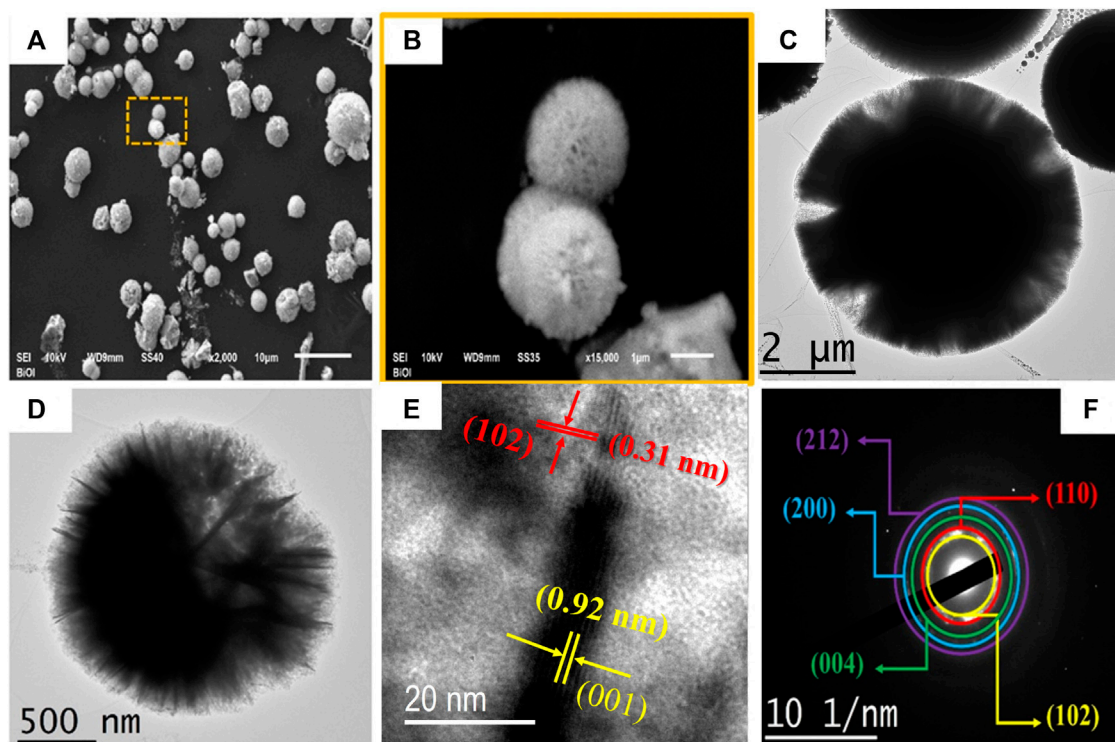
FIGURE 4
(A,B) SEM, **(C,D)** TEM, **(E)** HRTEM micrographs, and **(F)** SAED pattern of the BiOI.

optical absorption edges were shifted from 630 nm in BiOI to 650 nm in GO/BiOI. Besides, the loading of GO in BiOI enhanced the absorbance in the Vis-IR region, showing a background absorbance characteristic of carbonaceous-decorated photocatalysts. The, E_g values were determined by the Kubelka-Munk (K-M or F(R)) method, as described in Eq. 2:

$$F(R) = \frac{(1 - R)^2}{2R} \qquad (2)$$

where F(R) is equivalent to the extinction coefficient, and R is the reflectance.

From the modified K-M method, the F(R) was assessed by multiplying the photon energy ($h\nu$) using the corresponding n coefficient (1/2 for an indirect transition in BiOI) and applying the following expression: $(F(R)h\nu)^{\frac{1}{2}}$ vs. $h\nu$ (eV). The band gap, E_g, was determined by extrapolating the linear plot segment up to the x-axis intersection, as is shown in Figure 3B. The, E_g of BiOI and GO/BiOI were 2.07 and 1.96, respectively, consistent with reported, E_g values (Zhong et al., 2019; Jiang et al., 2021).

The morphological features of BiOI were examined by SEM and TEM. Figure 4A shows an SEM image at low magnification ratio, revealing highly symmetric BiOI microspheres with low agglomeration and particle sizes ranging from 2 to 10 μm. The SEM snapshot marked by the yellow dashed line in Figure 4B at higher magnification shows "flower-shaped" BiOI microspheres. Figures 4C, D expose BiOI microspheres composed of many nanosheets of atomic thickness radially assembled, corroborating the formation of a hierarchical flower-shaped porous structure. Microspheres are denser in the inner part, while a highly porous matrix is available on the radial

surface. This morphology is consistent with the textural properties evaluated from the N_2 adsorption-desorption isotherms. The flower-shaped configuration produces stable particles for photocatalytic applications. In Figures 4A, E high-resolution micrograph is shown, revealing the interplanar distances (d-spacing) of 0.92 and 0.31 nm, corresponding to the (001) and (102) planes of the BiOI crystal. Figure 4F displays the Selected Area Electron Diffraction (SAED) analysis. The appearance of diffracted rings revealed the polycrystalline nature of the BiOI. The crystalline planes identified in the SAED analysis correspond to (102), (110), (004), (200), and (212) Miller indices, measuring 0.301, 0.282, 0.228, 0.199, and 0.168 nm, respectively, confirming the tetragonal symmetry of BiOI. The interplanar distances measured by HRTEM and the SAED diffracted rings coincided with the crystallographic planes determined by XRD.

Figure 5 shows the textural and chemical composition analysis of GO/BiOI nanocomposite by TEM characterization. Figure 5A displays the GO electron shell of ~15 × 10 μm coated or covering about a dozen BiOI microspheres in the GO/BiOI nanocomposite. The microstructure of GO in contact with BiOI is advantageous in significantly diminishing the recombination of photogenerated electron-hole pairs during the photocatalytic process. The elemental mapping displays the expected presence of carbon, oxygen, bismuth, and iodine in the BiOI composite, as shown individually in Figures 5C–F.

Furthermore, the above microscopic findings are associated with the outcomes obtained from complementary techniques such as XRD, Raman, N_2 physisorption, and UV-Vis DRS spectroscopy. The interplanar distances observed through HRTEM as well as the diffracted rings acquired by SAED align remarkably well with the
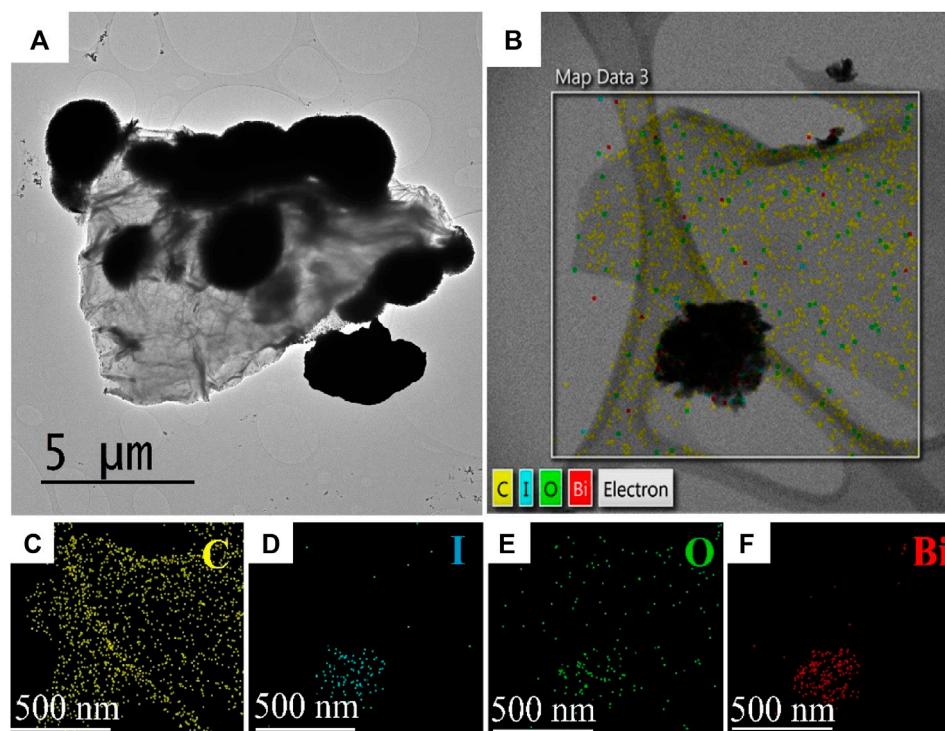
FIGURE 5
(A) TEM image, and **(B–F)** STEM-EDS analysis of the GO/BiOI.

crystallographic planes determined by XRD. Additionally, the homogeneity of the microsphere distribution observed by TEM and the high interaction between BiOI and GO phases are consistent with the textural properties, such as the S_{BET} area and the mesoporosity nature of the catalysts. The atomic distribution identified through elemental mapping relates to the optical properties and electronic structure revealed by UV-Vis DRS spectroscopy.

PL analysis is helpful to investigate the separation efficiency of the photogenerated pair ($e^- \text{-} h^+$) in the as-prepared catalysts. Figure 6A depicts the emission PL spectra of BiOI and GO/BiOI nanocomposites in the 400–600 nm wavelength interval. The weaker PL intensity of the spectrum indicates a lower possibility of photogenerated pair recombination. The PL spectrum intensity of BiOI was higher than that of GO/BiOI, showing superior separation charge in GO/BiOI since the GO acts as the e^--receptor, which hinders the recombination phenomenon and yields higher photocatalytic performance for this nanocomposite.

Figure 6B shows the adsorption isotherms of RhB on BiOI and GO/BiOI. The highest uptake of RhB adsorbed was 19 and 24 mg/g for BiOI and GO/BiOI, respectively. The adsorption capacity of GO/BiOI toward RhB was around 1.3 times higher than that of BiOI; the maximum adsorption capacity is related to the addition of GO since it increased the S_{BET} and adsorption sites available for RhB molecules compared to BiOI. Furthermore, the pH_{PZC} of BiOI and GO/BiOI were determined to be 5.40 and 5.13, respectively, confirming that the catalysts have negative surface charges at pH = 7. These results suggest that low additions of GO to BiOI are

sufficient to slightly shift the pH_{PZC} of GO/BiOI toward acidic values, thereby enhancing the attractive interaction between organic molecules and catalysts. It has been reported that GO possesses a high content of acidic sites (Carrales-Alvarado et al., 2020), as evidenced by the pH_{PZC} value obtained for GO/BiOI, promoting electrostatic attractions with the protonated amine group of the zwitterionic species of RhB (RhB$^\pm$), which predominates at pH = 7 according to the speciation diagram of RhB (Segovia-Sandoval et al., 2023).

The experimental data of the RhB adsorption equilibrium onto the photocatalysts were interpreted by the Langmuir isotherm model, Eq. 3:

$$q = \frac{q_m K C_e}{1 + K C_e} \tag{3}$$

where C_e is the equilibrium concentration of RhB, mg/L; K is the adsorption constant, L/mg; q_m is the maximum adsorption capacity, mg/g; q is the uptake adsorbed of the RhB on the photocatalysts, mg/g.

The parameters were determined employing a nonlinear least-squares optimization procedure and the Rosenbrock-Newton algorithm, and the average percentage deviation (%D) was assessed as follows, Eq. 4:

$$\%D = \left(\frac{1}{N} \sum_{i=1}^{N} \left| \frac{q_{i,exp} - q_{i,pred}}{q_{i,exp}} \right| \right) \times 100\% \tag{4}$$

where N is the number of experimental data; $q_{i,exp}$ is the experimental uptake adsorbed of RhB, mg/g; $q_{i,pred}$ is the uptake adsorbed of RhB computed by Langmuir isotherm, mg/g.
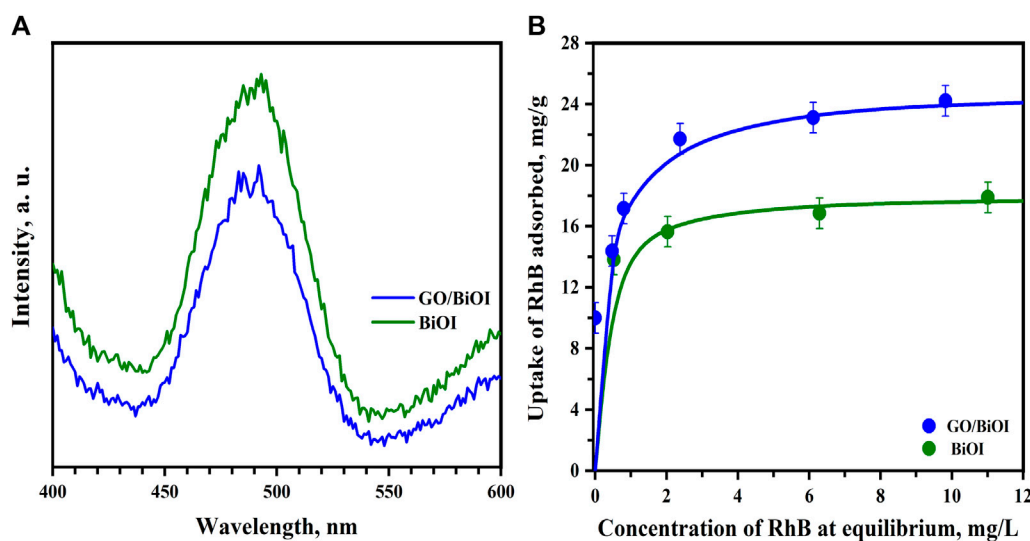
FIGURE 6
(A) PL spectra of the BiOI and GO/BiOI photocatalysts (334 nm as excitation wavelength), and **(B)** adsorption isotherms of RhB onto BiOI and GO/BiOI (pH = 7, 25°C, 500 rpm, 100 mg/100 mL dosage). The lines in **(B)** represent the prediction of the Langmuir isotherm, and the error bars indicate ±1 SD in the uptake of RhB adsorbed.

The obtained q_m parameter of the Langmuir isotherm were 18.03 and 24.78 mg/g, whereas the K was 5.63 and 2.89 L/mg for BiOI and GO/BiOI, respectively. The %D value for BiOI was 3.5% and 1% for GO/BiOI, revealing that the Langmuir isotherm predicted the experimental data quite well.

The Langmuir–Hinshelwood (H-L) model (Kumar et al., 2008) was used to interpret the experimental photodegradation rate data as follows, Eq. 5:

$$-r = -\frac{dC}{dt} = \frac{kKC}{1 + KC} \qquad (5)$$

where -r is the rate of photodegradation, mg/L min; k is the reaction rate constant, mg/L min; C is the pollutant (RhB) concentration, mg/L; K is the equilibrium constant of pollutant adsorption, L/mg.

The term kK can be represented as the apparent rate constant, k_{app} (min^{-1}). Most photocatalytic degradation studies are performed at low pollutant concentrations, and it can be assumed that $KC << 1$. Hence, the H-L model simplifies to a pseudo-first-order reaction rate, as shown in Eq. 6:

$$-\frac{dC}{dt} = k_{app}C \qquad (6)$$

where k_{app} is the first-order apparent rate constant, min^{-1}. Eq. 6 can be integrated into Eq. 7 employing the subsequent limits at $t = 0$, $C = C_0$ and $t > 0$, $C = C$:

$$C = C_0 e^{-k_{app}t} \qquad (7)$$

The initial rate of RhB photodegradation, -r_0, can be computed from Eq. 8:

$$-r_0 = k_{app}C_0 \qquad (8)$$

The k_{app} rate constant was ascertained by non-linear least-squares applying the Rosenbrock-Newton computational procedure. The goodness-of-fit for the kinetic model was evaluated by estimating the %D, Eq. 4, and the coefficient of determination, R^2. The RhB degradation percentage achieved by the BiOI-based catalysts was evaluated by Eq. 9, as follows:

$$\%X_{RhB} = \left(1 - \frac{C}{C_0}\right) \times 100\% \qquad (9)$$

The dimensionless concentration decay curves (C/C$_0$) of RhB for the BiOI and GO/BiOI photocatalytic degradation are depicted in Figure 7A. A non-photolysis experiment was performed without a catalyst, and the results confirmed that the direct photolysis of RhB molecule under 19 W white LED irradiation did not occur. At 240 min of LED irradiation, BiOI and GO/BiOI nanocomposites achieved a %X$_{RhB}$ of 52% and 100%, respectively. The k_{app} value of GO/BiOI is 4.8-fold higher than that of BiOI. Besides, the initial degradation rate (-r_0) of RhB photodegradation using GO/BiOI was 2.8-fold faster than BiOI (see Table 2). The enhanced photocatalytic performance of GO/BiOI is related to the incorporation of GO (3 wt.%) into the BiOI since the GO sheets act as e^--receptor, promoting the capture and transfer of electrons, which diminishes the recombination rate of the photogenerated pair, as demonstrated by PL analysis. In addition, the existence of GO increased the S_{BET} of GO/BiOI, improving the RhB adsorption onto the catalyst surface, consistent with the C$_0$ value at $t = 0$ min (See Table 2).

Supplementary Figure S1 depicts the UV-Vis absorbance spectra of the RhB solution samples taken out at different times during the visible photodegradation by GO/BiOI. The spectrum of RhB shows main signals around 554, 353, and 259 nm before adding GO/BiOI to the dye solution, represented as $t = -30$ min. After adding GO/BiOI to the RhB solution, the GO/BiOI-RhB suspension was stirred in the dark for 30 min to reach the
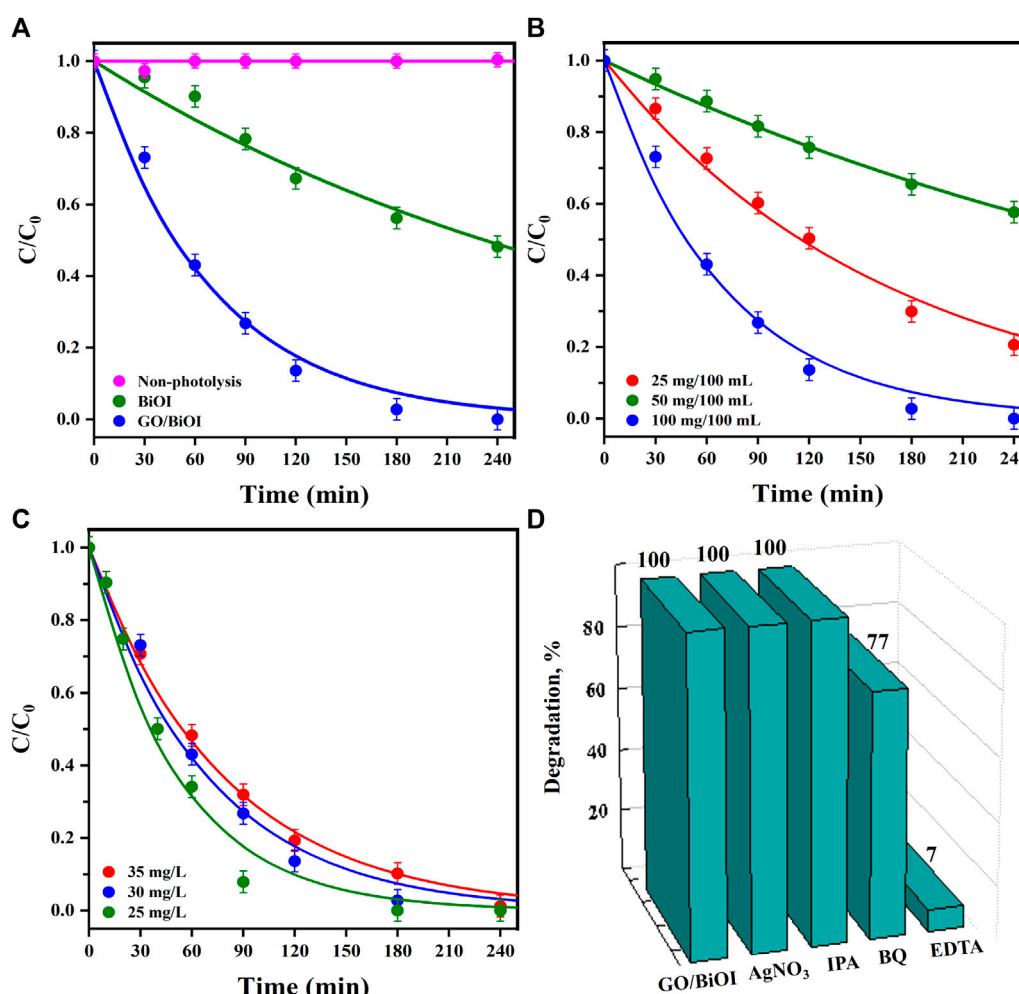
FIGURE 7
(A) Dimensionless concentration decay curves (C/C$_0$) vs. illumination time of RhB photodegradation using BiOI and GO/BiOI catalysts (pH = 7, 25°C, 30 mg/L RhB, 100 mg/100 mL dosage), **(B)** effect of the catalyst dosage (25/100, 50/100, 100/100 mg/mL), **(C)** effect of initial RhB concentration (25−35 mg/L RhB), and **(D)** addition of different scavengers (0.2 mM) on the performance of GO/BiOI. The solid lines in **(A−C)** represent the prediction of the pseudo-first-order kinetic model (Eq. 7), and the error bars indicate ±3 SD in RhB photodegradation.

adsorption equilibrium of RhB molecules on the GO/BiOI surface. The photodegradation process was initiated at t = 0 min when the white LED was turned on to induce the photoactivation of the catalyst and the photosensitization of the RhB molecules. During RhB degradation, the primary signal at 554 nm at t = 0 min progressively shifted toward 525 nm at t = 90 min, which is related to the gradual N-demethylation of the dye molecule (hypsochromic shift) and the formation of other by-products. At t = 240 min, no RhB signals were observed, confirming its complete degradation.

The mineralization of RhB during the photodegradation was calculated as follows, Eq. 10:

$$Mineralization\,degree\,(\%) = \left(\frac{TOC_0 - TOC}{TOC_0}\right) \times 100\% \quad (10)$$

Supplementary Figure S2 illustrates the removal of RhB from an aqueous solution in terms of TOC concentration using GO/BiOI.

The photocatalytic efficiency determined was 70% after 240 min of visible LED irradiation, concerning the TOC value measured for the initial RhB concentration (t = −30 min).

It is well known that solution pH affects the surface charge of catalysts and the ionization degree of pollutants. As a function of solution pH, the RhB molecule can exist in a couple of species; the cationic RhB species (RhB$^+$) prevails at pH lower than its dissociation constant (pK$_a$ ≈ 3.7), while the zwitterionic species (RhB$^\pm$) predominates at pH solutions higher than the pK$_a$ value. In addition, if the pH of the solution is less than the pH$_{PZC}$ of GO/BiOI (pH$_{PZC}$ = 5.13), the catalyst surface is positively charged. Conversely, at a pH above pH$_{PZC}$, the catalyst surface becomes negatively charged. According to this, at pH = 3, the positively charged surface of GO/BiOI and RhB$^+$ species induces the electrostatic repulsion, hindering adsorption and photodegradation. On the other hand, at pH = 7, the RhB$^\pm$ species are adsorbed onto GO/BiOI by electrostatic attraction involving the negative charge of the catalyst surface and the

TABLE 2 RhB percentage degradation (%X$_{RhB}$), the first-order rate constant (k$_{app}$), RhB initial concentration (C$_0$, after attaining the RhB adsorption equilibrium), initial reaction rate (-r$_0$) of RhB photodegradation using BiOI and GO/BiOI photocatalysts irradiated with 19 W white LED. In addition, the GO/BiOI catalyst under different experimental conditions and scavenger assays.

Photocatalysts (PC) 100 mg PC; 30 mg/L RhB	%X$_{RhB}$ t = 240 min	k_{app} × 10^{-2} (min^{-1})	C$_0$ (mg/L)	-r_0×10^{-2} (mg/L min)	%D	R^2
Non-photolysis	0	-	30.00	-	-	-
BiOI	52	0.298	11.01	3.281	3.8	0.984
GO/BiOI	100	1.443	6.44	9.293	3.3	0.993
Photocatalyst dosage GO/BiOI	%X$_{RhB}$ t = 240 min	k_{app}×10^{-2} (min^{-1})	C$_0$ (mg/L)	-r_0×10^{-2} (mg/L min)	%D	R^2
25/100 mg/mL	42	0.229	21.26	4.868	1.0	0.998
50/100 mg/mL	79	0.602	15.33	9.229	2.9	0.995
100/100 mg/mL	100	1.443	6.44	9.293	3.3	0.993
RhB concentration (t = - 30 min)						
25 mg/L	100	1.926	2.97	5.720	6.6	0.986
30 mg/L	100	1.443	6.44	9.293	2.9	0.993
35 mg/L	99	1.273	10.30	13.111	3.3	0.998
Scavengers						
EDTA-Na$_2$	7	0.016	26.38	0.422	1.5	0.723
BQ	77	1.233	3.46	4.266	10.6	0.940
IPA	100	1.571	3.56	5.593	7.7	0.988
AgNO$_3$	100	-	2.22	-	-	-
Reuse cycles						
1st	100	1.443	6.44	9.293	3.3	0.993
2nd	95	1.196	8.16	9.759	3.9	0.991
3rd	86	0.864	11.03	9.530	6.6	0.988

TABLE 3 Compilation of RhB photodegradation over different BiOI-based catalysts and the GO/BiOI as-prepared in this work.

Catalyst	Experimental conditions		Photocatalytic efficiency			
	Catalyst dosage and RhB concentration (mg/mL; mg/L)	Light source, W	Degradation; time (%; min)	k_{app} × 10^{-2} (min^{-1})	Rated power of system (kWh)	Ref.
BN/BiOI (0.5 wt% of BN)	100/100; 10	Xe lamp, 350	93; 100	2.291	0.58	Liu et al. (2016)
NCC/BiOI	30/-; 20	Xe lamp, 500	92; 120	0.938	1.00	Hou et al. (2019)
BiOBr/BiOI (3:1 mol ratio)	35/100; 20	Xe lamp, 500	100; 80	7.120	0.67	Li et al. (2019)
GO/BiOI (3 wt% of GO)	100/100; 50	Xe lamp, 300	95; 120	2.360	0.60	Zhong et al. (2019)
GO/BiOI (1.5 wt% of GO)	100/100; 5	Hg lamp, 125	35; 80	0.560	0.17	Xia et al. (2020)
AC/BiOI (3.3 wt% of AC)	10/50; 10	Xe lamp, 500	95; 120	2.350	1.00	Hou et al. (2017)
GO/BiOI (3 wt% of GO)	100/100; 30	78 white LEDs, 19	100; 240	1.443	0.08	This study

protonated amine groups of the RhB$^{\pm}$ molecule, promoting its degradation.

Table 3 summarizes the results of some investigations related to similar BiOI-based catalysts applied to RhB degradation. It is worth mentioning that the %X$_{RhB}$ achieved using the low-power (19 W) and the straightforward LED array was superior to many of the %X$_{RhB}$ reported in the literature that use high-power light sources, especially considering the rated power consumption of the photocatalytic reactor (kWh). For example, the LED-based photoreactor in this research exhibited a remarkable performance by completely degrading 30 mg/L

RhB ($\%X_{RhB} = 100\%$) and consuming only 0.08 kWh, which is at least 2 times lower than the rated power employed to degrade a 6-fold lower concentration of RhB and attaining a $\%X_{RhB}$ of 55% (Xia et al., 2020). Only this work and a previous work by Li et al. (2019) achieved the complete degradation of RhB; however, the rated power consumed in this work was 8.4 times lower than in the other work. In general, the photodegradation of RhB was conducted more efficiently with the GO/BiOI synthesized in this work.

Figure 7B shows the effect of GO/BiOI dosage (mass/volume) on the photodegradation of RhB solution with an initial concentration of 30 mg RhB/L. For a GO/BiOI dosage of 100/100 mg/mL, the k_{app} was 2.4 and 6.3-fold faster than 50/100 and 25/100 mg/mL, respectively. The $\%X_{RhB}$ was 100, 79% and 42% for 100/100, 50/100 and 25/100 dosages, whereas the $-r_0$ of RhB degradation was 1.9-fold slower for 25/100 mg/mL compared to 100/100 mg/mL (see Table 2). The photocatalytic activity of GO/BiOI diminished as the photocatalyst dosage decreased because fewer catalyst particles were available for photon absorption, producing fewer oxidative species to degrade the same concentration of RhB molecules, as well as the mass of RhB adsorbed on the catalyst surface decreased due to the reduction in the available active sites. No further dosages were employed since it has been reported that solution turbidity increases and light scattering effects can be enhanced, diminishing the degradation efficiency of the target molecule (Madihi-Bidgoli et al., 2021; Moral-Rodriguez et al., 2022).

Figure 7C displays the impact of RhB concentration ($t = -30$ min) on the photocatalytic performance of GO/BiOI.

The $\%X_{RhB}$ registered a slight variation, 99%–100%, for the initial concentration range of 35–25 mg/mL RhB, demonstrating that dye degradation is nondependent on the initial concentration. However, the $-r_0$ of RhB photodegradation for the 35 mg/mL concentration was 1.4 and 2.3-fold faster than for 30 and 25 mg/mL, respectively.

Scavenger assays depicted in Figure 7D demonstrated that the main oxidative species in RhB degradation are holes (h^+) and superoxides ($O_2^{\bullet-}$) since the addition of EDTA-Na$_2$ and BQ to the reaction system reduced the $\%X_{RhB}$ to 7% and 77%, respectively, compared to 100% previously registered without loading any reagent as trapping radicals. Besides, supplementing IPA and AgNO$_3$ to trap hydroxyl radicals ($^\bullet OH$) and electrons (e^-) did not play a significant role in RhB oxidation since the $\%X_{RhB}$ achieved was 100% in both cases. The influence of oxidative species in the photodegradation of RhB decreases in the following order: $h^+> O_2^{\bullet-}$.

Supplementary Figure S3 illustrates the reuse cycles performed for GO/BiOI. At 720 min, the $\%X_{RhB}$ was 86%, representing a 14% reduction in RhB degradation compared to the 100% obtained at 240 min. Moreover, the k_{app} obtained for the third cycle was 1.67 times lower than that of the first cycle, while the $-r_0$ of RhB degradation was almost constant in the three photocatalytic reuses (see Table 2). The decrease in k_{app} and $\%X_{RhB}$ in the third cycle is related to the RhB molecules remaining adsorbed on the surface of GO/BiOI, confirmed by the C_0 values registered for each cycle after adsorption in the dark. The RhB molecules adsorbed reduce the number of active sites available for adsorption, which affects the
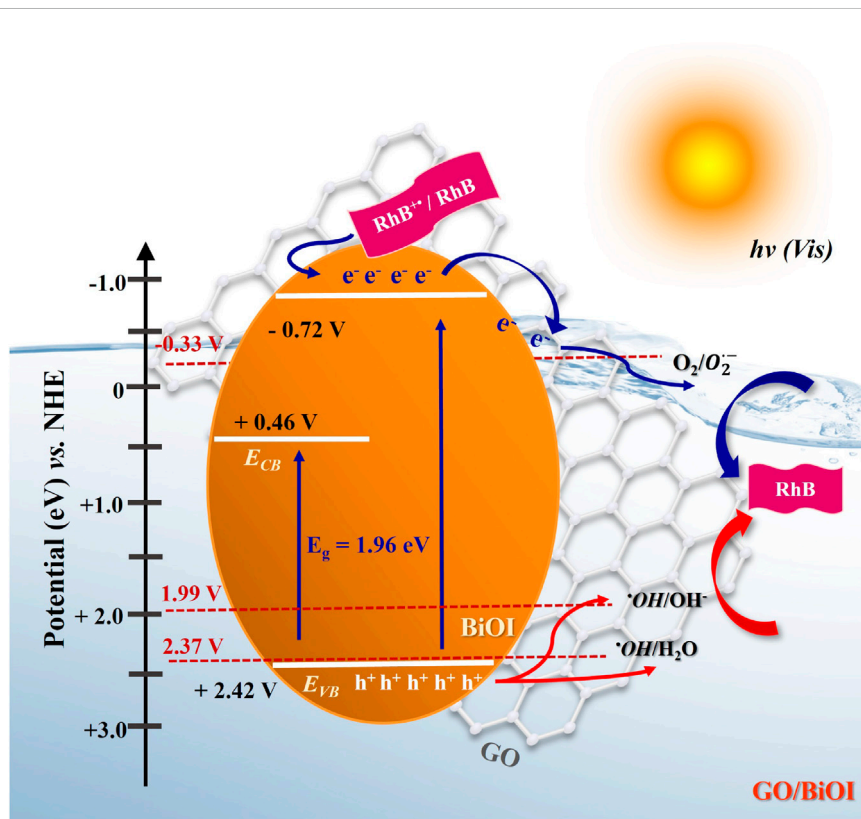
FIGURE 8
The postulated mechanism of RhB photodegradation using GO/BiOI under visible LED illumination.
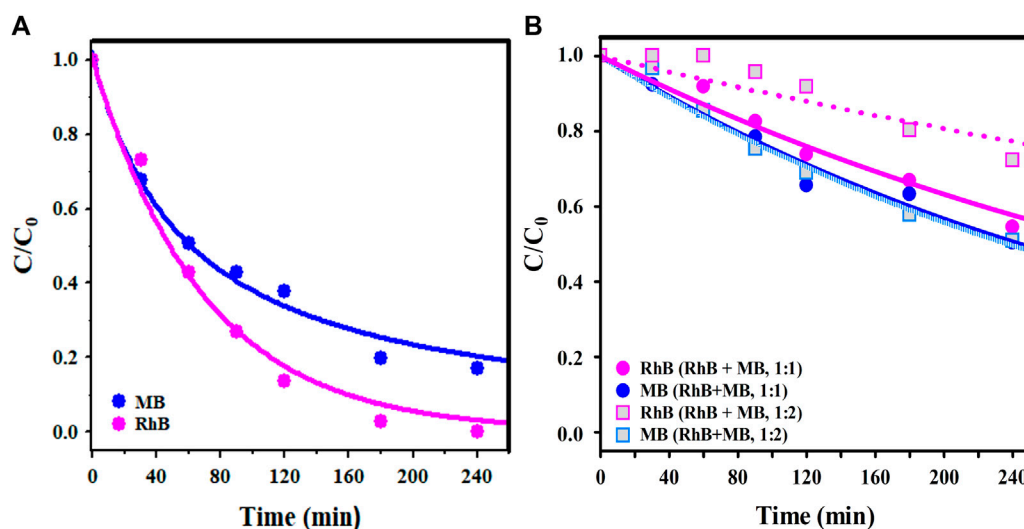
FIGURE 9
(A) C/C$_0$ curves vs. illumination time of MB and RhB photodegradation using GO/BiOI in single dye solutions (pH = 7, 25°C, 30 mg/L RhB or MB, 100/100 mg/mL dosage), and **(B)** RhB + MB mixed dye solutions (RhB/MB molar ratios of 1:1 and 1:2). The lines represent the prediction of the pseudo-first-order kinetic model (Eq. 7).

efficiency of RhB degradation. Although the %X$_{RhB}$ decreased in the third cycle, the GO/BiOI nanocomposite shows capacity for reuse considering the global removal of RhB in three cycles and according to the high initial concentration of RhB used in each cycle, 30 mg/L.

It is well known that the efficiency of pollutant degradation is affected by the, E_g value of the catalyst, the charge transfer process of the photogenerated pair (e^--h^+) and the subsequent production of the oxidative species. The effect of the transfer of e^--h^+ photogenerated and the generation of oxidative species from GO/BiOI on the RhB degradation can be analyzed by determining the conduction band energy (E_{CB}) and valence band energy (E_{VB}) potentials of GO/BiOI, which were assessed using Eqs 10, 11 as follows:

$$E_{CB} = X - E^e - \frac{1}{2}E_g \quad (11)$$

$$E_{VB} = E_{CB} + E_g \quad (12)$$

where X is the electronegativity of the constituent atoms in the BiOI compound, 5.94 eV; E^e is the energy of the electrons in the hydrogen scale, 4.5 eV vs. Normal Hydrogen Electrode (NHE); E_g is the experimental energy gap of BiOI, eV. The E_{CB} and E_{VB} potentials were assessed as 0.46 and 2.42 V, respectively.

Figure 8 illustrates the postulated mechanism of RhB degradation on the GO/BiOI photocatalyst. By irradiating BiOI under visible LED (λ > 420 nm), photoinduced electrons (e^-) in the valence band (VB) can be promoted to the conduction band (CB), and then e^- can be excited to a higher potential E$_{CB}$ (−0.72 V) (Jiang et al., 2021); this e^- promotion leaves photogenerated holes (h^+) in the VB of BiOI. The E$_{CB}$ of BiOI (−0.72 V) is more negative than the O$_2$/O$_2^{•-}$ potential (−0.33 V) (Mousavi et al., 2016), allowing the active e^- to be transferred to the GO sheets that act as e^--receivers, reducing the O$_2$ to O$_2^{•-}$ radical. Besides, the light photosensitizes the RhB molecules adsorbed on the surface of BiOI, leading to an excited state of RhB (RhB$^{+•}$), which enhances the transfer of e^- from RhB$^{+•}$ to the CB of BiOI. Furthermore,

the E$_{VB}$ of BiOI (2.42 V) is more positive than the potentials of $^•$OH/H$_2$O and $^•$OH/OH$^-$ (2.37 V and 1.99 V, respectively (Yu et al., 2015; Huang et al., 2017)), promoting that the h^+ in VB could directly oxidize the RhB molecule or OH$^-$ to produce $^•$OH radicals. Thus, the generated h^+ and O$_2^{•-}$ radicals can degrade RhB, which is consistent with the results of the scavenger assays.

Figure 9A depicts the activity of GO/BiOI in the simultaneous photodegradation of MB and RhB, and the %X$_{Dye}$, k_{app} rate constants, and -r_0 values are compiled in Table 4. The %X$_{MB}$ in a single MB solution was 80% compared to 100% achieved in the case of RhB. The k_{app} of MB degradation was 1.9-fold lower than RhB, and the -r_0 of MB photodegradation was 11.6-fold slower than that of RhB. In a binary RhB + MB solution (1:1 M ratio) using GO/BiOI, the %X$_{RhB}$ and %X$_{MB}$ were 45% and 50%, respectively, diminishing 2.2 and 1.6-fold compared to the RhB and MB degradation accomplished in single dye solutions, as depicted in Figure 9B. By increasing the MB concentration in the MB + RhB binary solution to a 2:1 M ratio, the %X$_{MB}$ and %X$_{RhB}$ were 49% and 28%, respectively; the %X$_{MB}$ was less than that obtained in the 1:1 M ratio binary solution, indicating higher affinity of GO/BiOI towards RhB degradation. Even though the MB adsorption onto GO/BiOI is higher at pH 7 due to the cationic MB (MB$^+$) species, the photodegradation of the zwitterionic RhB molecule is superior in binary solutions (see C$_0$ in Table 4). Herein, the -r_0 of RhB degradation is higher than those obtained for MB in binary solutions.

Figure 10A depicts the H$_2$ production profiles obtained for BiOI, GO/BiOI and GO photocatalysts. The BiOI showed the lowest activity after 5 h of irradiation, and the GO/BiOI exhibited slightly higher activity than GO. The BiOI produced an average of 323.25 μmol/h·g H$_2$ under UV light using a 2 W pen-ray lamp, and by loading 3 wt.% of GO onto this photocatalyst, the H$_2$ production increased up to 509.61 μmol/h g, as illustrated in Figure 10B. The H$_2$ production increased, showing that the GO/

TABLE 4 The %X_{RhB}, k_{app}, -r_0, %D and R^2 for the photodegradation of RhB and MB single dye solutions and RhB + MB binary solutions (1:1 and 1:2 M ratio) over the GO/BiOI catalyst (100 mg PC/100 mL dye).

Dye	%X_{Dye} t = 240 min	k_{app} × 10^{-2} (min^{-1})	C_0 (mg/L)	-r_0×10^{-2} (mg/L min)	%D	R^2
RhB	100	1.443	6.44	9.293	3.3	0.993
MB	80	0.757	1.06	0.802	6.8	0.995
RhB (RhB + MB, 1:1)	45	0.229	14.26	3.265	3.3	0.976
MB (RhB + MB, 1:1)	50	0.284	2.20	0.625	2.5	0.988
RhB (RhB + MB, 1:2)	49	0.291	9.45	2.750	2.3	0.991
MB (RhB + MB, 1:2)	28	0.107	2.72	0.291	4.1	0.915

FIGURE 10
(A) Profile of H2 production by photocatalysts under 2 W UV light, and (B) H2 production in μmol/g at 1 h (50% V/V methanol-water, 25 mg catalyst). The H2 production rate from the methanol-water solution without using catalysts was 61.96 μmol/h g. Error bars in (B) represent the standard deviation of H2 production, ±7.
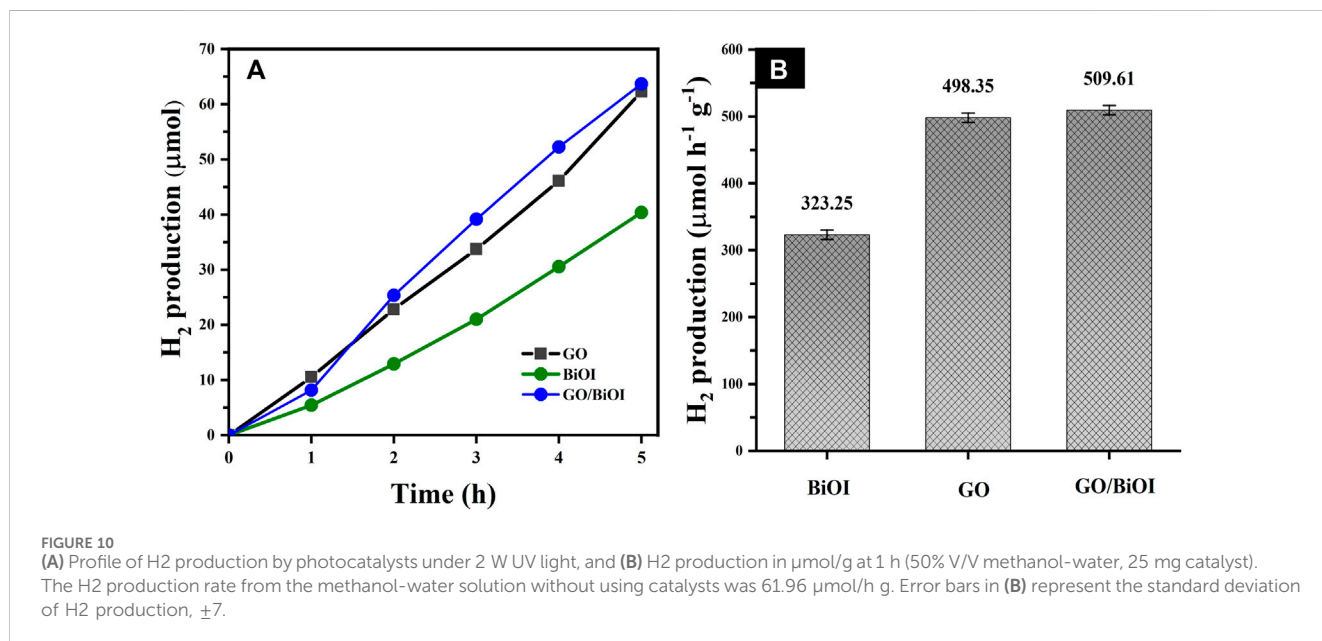
TABLE 5 Compilation of H$_2$ production over different BiOI-based catalysts and the GO/BiOI as-synthesized in this work.

Catalyst	Experimental conditions			Photocatalytic efficiency		Ref.
	Catalyst mass (mg)	Sacrificial reagent	Illumination source, W	Hydrogen production (μmol/ h g)	Rated power of the system (kWh)	
BiOI films	-	Calcium gluconate	Vis LED, 20	1800	0.020	Luevano-Hipólito et al. (2023)
K-BiOI	20	Methanol	Xe, 300	6,510	0.300	Yang et al. (2021)
BiOI/β-Bi$_2$O$_3$	5	Sodium sulfite	Xe, 300	91	0.300	Shan et al. (2024)
G/AgI/BiOI	50	Sodium chloride sodium sulfite	Hg, 300	183	0.300	Chang et al. (2019)
ZnSn(OH)$_6$/ BiOI	50	Ethanol	Hg, 125 Halide, 400	150 82	0.130 0.400	Li et al. (2013)
Zr-MOF NU-1000/BiOI	10	Triethanolamine	Vis LED, 100	610	0.100	Li et al. (2021)
Bi^0/BiOI/CdS	50	Lactic acid	Xe, 300	36,000	0.300	Zhou et al. (2021)
GO/BiOI	50	Methanol	Hg, 2	509	0.002	This work

BiOI is a more efficient photocatalyst, producing 63% more hydrogen than the pristine BiOI. This improvement in photoactivity is achieved by inserting GO into the BiOI, where the graphene sheets act as an electron sink, avoiding recombination and promoting the flow of electrons from the BiOI to the GO to align the Fermi level (Liu et al., 2013). Furthermore, the better performance of GO/BiOI can be related to its higher S_{BET} area ($46 \, m^2/g$) compared to that of the BiOI ($38 \, m^2/g$) and GO ($13 \, m^2/g$). The H_2 production by GO is similar to that of GO/BiOI, which is related to its outstanding physicochemical properties; however, the low-yield synthesis of GO limits its use as a bare photocatalyst. It is worth mentioning that the H_2 output attained by BiOI-based catalysts in this research was carried out without the assistance of a co-catalyst.

Although high H_2 production over BiOI films and heterojunctions has been reported previously, the irradiation lamp used in this study consumes lower power (2 W), which represents a substantial energy saving compared to Xe, Hg, or LED illumination sources applied to produce H_2 by water splitting; especially when comparing the rated power of the system (kWh) vs. H_2 production ($\mu mol/h \, g$), Table 5. For example, 0.300 kWh was required to produce 91 $\mu mol/h \, g$ of H_2 using BiOI/β-Bi_2O_3 (Shan et al., 2024), which is 150 times more kWh and 5.6 times less H_2 production than in the present research. In addition, 183 $\mu mol/h \, g$ of H_2 was attained with 0.300 kWh over G/AgI/BiOI heterojunction (Chang et al., 2019), indicating a 2.8-fold lower H_2 output and 150-fold higher nominal rated power of the system compared to this work.

4 Conclusion

The as-prepared hierarchical BiOI and GO/BiOI microspheres exhibited satisfactory morphological, textural, and optical properties determined by various characterization techniques, consolidating a comprehensive understanding of their high photoactivity and efficient enhancement of catalytic performance induced with very low power light sources.

In particular, the BiOI and GO/BiOI photocatalysts achieved a % X_{RhB} of 52% and 100%, respectively, within 240 min of irradiation with a simple 19 W white LED array. Herein, the %X_{RhB} attained by GO/BiOI is remarkably superior to previous studies regarding nominal power consumption vs. RhB degradation efficiency. GO/BiOI dosage showed an essential role in the RhB photodegradation, and the k_{app} for using a GO/BiOI dosage of 100/100 mg/mL was 2.4 and 6.3-fold faster than 50/100 and 25/100 mg/mL, whereas the initial RhB concentration (35–25 mg/mL) did not exhibit a considerable effect on the performance of GO/BiOI. Scavenger assays have confirmed that the main species causing the RhB oxidation are h^+ and $O_2^{\bullet-}$. For the photodegradation of RhB using GO/BiOI, the degree of RhB mineralization determined by TOC analysis was 70%, and this catalyst can be efficiently utilized in photocatalytic cycles. In addition, the %X_{MB} over the GO/BiOI was 80%; the k_{app} of MB degradation was 1.9-fold less than RhB, whereas the -r_0 of RhB photodegradation was 11.6-fold faster than MB. In RhB + MB binary solutions, the higher affinity of GO/BiOI towards RhB degradation was confirmed, and the performance of GO/BiOI was about 2-fold lower than in a single RhB solution.

Furthermore, the H_2 production by BiOI-based photocatalysts and GO was increased in the following order: BiOI < GO < GO/BiOI. The GO/BiOI produced an average of 509.61 $\mu mol/h \cdot g \, H_2$ under 2 W UV lamp irradiation. The GO acting as electron skin enhanced the photocatalytic performance of BiOI. GO is an excellent electron receptor, diminishing the recombination rate of the photogenerated pair ($e^- - h^+$) in the GO/BiOI composite.

Data availability statement

The raw data supporting the conclusion of this article will be made available by the authors, without undue reservation.

Author contributions

SO-R: Conceptualization, Data curation, Formal Analysis, Investigation, Methodology, Validation, Writing–original draft, Writing–review and editing. HO-G: Data curation, Formal Analysis, Investigation, Writing–original draft, Writing–review and editing. MQ: Conceptualization, Formal Analysis, Investigation, Supervision, Writing–original draft, Writing–review and editing. RL-R: Conceptualization, Data curation, Formal Analysis, Investigation, Methodology, Writing–original draft, Writing–review and editing. AM-R: Conceptualization, Data curation, Formal Analysis, Investigation, Methodology, Writing–original draft. EM-M: Conceptualization, Data curation, Formal Analysis, Funding acquisition, Investigation, Methodology, Project administration, Resources, Supervision, Validation, Visualization, Writing–original draft, Writing–review and editing.

Conflict of interest

The authors declare that the research was conducted in the absence of any commercial or financial relationships that could be construed as a potential conflict of interest.

The author(s) declared that they were an editorial board member of Frontiers, at the time of submission. This had no impact on the peer review process and the final decision.

Publisher's note

All claims expressed in this article are solely those of the authors and do not necessarily represent those of their affiliated organizations, or those of the publisher, the editors and the reviewers. Any product that may be evaluated in this article, or claim that may be made by its manufacturer, is not guaranteed or endorsed by the publisher.

Supplementary material

The Supplementary Material for this article can be found online at: https://www.frontiersin.org/articles/10.3389/fnano.2024.1388458/full#supplementary-material

References

Abdullah, H., Khan, M. M. R., Ong, H. R., and Yaakob, Z. (2017). Modified TiO_2 photocatalyst for CO_2 photocatalytic reduction: an overview. *J. CO2 Util.* 22, 15–32. doi:10.1016/j.jcou.2017.08.004

Arumugam, M., and Choi, M. Y. (2020). Recent progress on bismuth oxyiodide (BiOI) photocatalyst for environmental remediation. *J. Ind. Eng. Chem.* 81, 237–268. doi:10.1016/j.jiec.2019.09.013

Bannisher, F. A. (1935). The crystal-structure of the bismuth oxyhalides. *Mineral. Mag.* 24, 49–58. doi:10.1180/minmag.1935.024.149.01

Barrett, E. P., Joyner, L. G., and Halenda, P. P. (1951). The Determination of pore volume and area distributions in porous substances. I. Computations from Nitrogen Isotherms. *J. Am. Chem. Soc.* 73, 373–380. doi:10.1021/ja01145a126

Brunauer, S., Emmett, P. H., and Teller, E. (1938). Adsorption of gases in multimolecular layers. *J. Am. Chem. Soc.* 60, 309–319. doi:10.1021/ja01269a023

Carrales-Alvarado, D. H., Rodríguez-Ramos, I., Leyva-Ramos, R., Mendoza-Mendoza, E., and Villela-Martínez, D. E. (2020). Effect of surface area and physical–chemical properties of graphite and graphene-based materials on their adsorption capacity towards metronidazole and trimethoprim antibiotics in aqueous solution. *Chem. Eng. J.* 402, 126155. doi:10.1016/j.cej.2020.126155

Chang, C. J., Yan-Gu, L., Chao, P. Y., and Chen, J. K. (2019). AgI-BiOI-graphene composite photocatalysts with enhanced interfacial charge transfer and photocatalytic H2 production activity. *Appl. Surf. Sci.* 469, 703–712. doi:10.1016/j.apsusc.2018.11.081

Gómez-Narváez, B., Mendoza-Mendoza, E., Peralta-Rodríguez, R. D., Bach, H., Barriga-Castro, E. D., Segovia-Sandoval, S. J., et al. (2024). Visible-LEDs-induced enhanced photocatalytic and antibacterial activity of $BiVO_4$-based green photocatalysts decorated with silver and graphene. *J. Photochem Photobio A* 447, 115191. doi:10.1016/j.jphotochem.2023.115191

Hassani, A., Krishanan, S., Scaria, J., Eghbali, P., and Nidheesh, P. V. (2021). Z-scheme photocatalysts for visible-light-driven pollutants degradation: a review on recent advancements. *Curr. Opin. Solid State Mat. Sci.* 25, 100941. doi:10.1016/j.cossms.2021.100941

Hou, J., Jiang, K., Shen, M., Wei, R., Wu, X., Idrees, F., et al. (2017). Micro and nano hierachical structures of BiOI/activated carbon for efficient visible-light-photocatalytic reactions. *Sci. Rep.* 7, 11665. doi:10.1038/s41598-017-12266-x

Hou, J., Jiang, T., Wei, R., Idrees, F., and Bahnemann, D. (2019). Ultrathin-layer structure of BiOI microspheres decorated on N-doped biochar with efficient photocatalytic activity. *Front. Chem.* 7, 378. doi:10.3389/fchem.2019.00378

How, G. T. S., Pandikumar, A., Ming, N. M., and Ngee, L. H. (2014). Highly exposed {001} facets of titanium dioxide modified with reduced graphene oxide for dopamine sensing. *Sci. Rep.* 4, 5044. doi:10.1038/srep05044

Huang, H., Huang, N., Wang, Z., Xia, G., Chen, M., He, L., et al. (2017). Room-temperature synthesis of carnation-like ZnO@AgI hierarchical nanostructures assembled by AgI nanoparticles-decorated ZnO nanosheets with enhanced visible light photocatalytic activity. *J. Colloid Interf. Sci.* 502, 77–88. doi:10.1016/j.jcis.2017.04.080

Jiang, W., Li, Z., Liu, C., Wang, D., Yan, G., Liu, B., et al. (2021). Enhanced visible-light-induced photocatalytic degradation of tetracycline using BiOI/MIL-125(Ti) composite photocatalyst. *J. Alloy Compd.* 854, 157166. doi:10.1016/j.jallcom.2020.157166

Ke, T., Guo, H., Zhang, Y., and Liu, Y. (2017). Photoreduction of Cr(VI) in water using $BiVO_4$-Fe_3O_4 nano-photocatalyst under visible light irradiation. *Environ Sci Pollut Res* 24, 28239–28247. doi:10.1007/s11356-017-0255-0

Kumar, K. V., Podoki, K., and Rocha, F. (2008). Langmuir-Hinshelwood kinetics – a theoretical study. *Catal. Commun.* 9, 82–84. doi:10.1016/j.catcom.2007.05.019

Li, H., Cui, Y., Hong, W., and Xu, B. (2013). Enhanced photocatalytic activities of $BiOI/ZnSn(OH)_6$ composites towards the degradation of phenol and photocatalytic H2 production (2013). *Chem. Eng. J.* 28, 1110–1120. doi:10.1016/j.cej.2013.05.086

Li, J., Yang, F., Zhou, Q., Wu, L., Li, W., Ren, R., et al. (2019). Visible-light photocatalytic performance, recovery and degradation mechanism of ternary magnetic Fe_3O_4/BiOBr/BiOI composite. *RSC Adv.* 9 (41), 23545–23553. doi:10.1039/c9ra04412d

Li, X., Gao, K., Mo, B., Tang, J., Wu, J., and Hou, H. (2021). BiOI particles confined into Metal-Organic Framework NU-1000 for valid Photocatalytic hydrogen Evolution under Visible light irradiation. *Inorg. Chem.* 60, 1352–1358. doi:10.1021/acs.inorgchem.0c02423

Liu, D., Jiang, Z., Zhu, C., Qian, K., Wu, Z., and Xie, J. (2016). Graphene-analogue BN-modified microspherical BiOI photocatalysts driven by visible light. *Dalton Trans.* 45, 2505–2516. doi:10.1039/c5dt03408f

Liu, H., Cao, W. R., Su, Y., Chen, Z., and Wang, Y. (2013). Bismuth oxyiodide–graphene nanocomposites with high visible light photocatalytic activity. *J. Colloid Interf. Sci.* 398, 161–167. doi:10.1016/j.jcis.2013.02.007

Luévano-Hipólito, E., Torres-Alvarez, D. A., and Torres-Martínez, L. M. (2023). Flexible BIOI thin films photocatalysts toward renewable solar fuels production. *J. Environ. Chem. Eng.* 11, 109557. doi:10.1016/j.jece.2023.109557

Madihi-Bidgoli, S., Asadnezhad, S., Yaghoot-Nezhad, A., and Hassani, A. (2021). Azurobine degradation using Fe_2O_3@multi-walled carbon nanotube activated peroxymonosulfate (PMS) under UVA-LED irradiation: performance, mechanism and environmental application. *J. Environ. Chem. Eng.* 9, 106660. doi:10.1016/j.jece.2021.106660

Moral-Rodríguez, A. I., Quintana, M., Leyva-Ramos, R., Ojeda-Galván, H. J., Oros-Ruiz, S., Peralta-Rodríguez, R. D., et al. (2022). Novel and green synthesis of $BiVO_4$ and $GO/BiVO_4$ photocatalysts for efficient dyes degradation under blue LED illumination. *Ceram. Int.* 48, 1264–1276. doi:10.1016/j.ceramint.2021.09.211

Mousavi, M., Habibi-Yangjeh, A., and Abitorabi, M. (2016). Fabrication of novel magnetically separable nanocomposites using graphitic carbon nitride, silver phosphate and silver chloride and their applications in photocatalytic removal of different pollutants using visible-light irradiation. *J. Colloid Interface Sci.* 480, 218–231. doi:10.1016/j.jcis.2016.07.021

Porter, J. J. (1973) *A study of the photodegradation of commercial dyes*. Washington: US Environmental Protection Agency, 93–94.

Putri, A. A., Kato, S., Kishi, N., and Soga, T. (2019). Relevance of precursor molarity in the prepared bismuth oxyiodide films by successive ionic layer adsorption and reaction for solar cell application. *J. Sci-Adv Mater Dev.* 4, 116–124. doi:10.1016/j.jsamd.2019.01.007

Quiroz-Cardoso, O., Oros-Ruiz, S., Gómez, S., López, R., and Gómez, R. (2019). Enhanced photocatalytic hydrogen production by CdS nanofibers modified with graphene oxide and nickel nanoparticles under visible light. *Fuel* 237, 227–235. doi:10.1016/J.fuel.2018.10.013

Rouquerol, F., Rouquerol, J., Sing, S. K. W., Llewellyn, P., and Maurin, G. (2014) *Adsorption by powders and porous solids: principles, methodology and applications*. Oxford: Elsevier.

Santamaría-Juárez, G., Gómez-Barojas, E., Quiroga-González, E., Sánchez-Mora, E., Quintana-Ruiz, M., and Santamaría-Juárez, J. D. (2019). Safer modified Hummers' method for the synthesis of graphene oxide with high quality and high yield. *Mater Res. Express* 6, 125631. doi:10.1088/2053-1591/ab4cbf

Saxena, R., Saxena, M., and Lochab, A. (2020). Recent progress in nanomaterials for adsorptive removal of organic contaminants from wastewater. *ChemistrySelect* 5, 335–353. doi:10.1002/slct.201903542

Segovia-Sandoval, S. J., Mendoza-Mendoza, E., Jacobo-Azuara, A., Jiménez-López, B. A., and Hernández-Arteaga, A. C. (2023). Highly efficient visible-LED-driven photocatalytic degradation of tetracycline and rhodamine B over Bi_2WO_6/$BiVO_4$ heterostructures decorated with silver and graphene synthesized by a novel green method. *Environ. Sci. Pollut. Res.* doi:10.1007/S11356-023-27731-6

Shan, L., Fang, Z., Ding, G., Shi, G., Dong, L., Li, D., et al. (2024). Electron confinement promoted the electric double layer effect of BiOI/β-Bi_2O_3 in

photocatalytic water splitting. *J. Colloid Interf. Sci.* 653, 94–107. doi:10.1016/j.jcis.2023.09.059

Si, Y., Chen, Y., Fu, Y., Zhang, X., Zuo, F., Zhang, T., et al. (2020). Hierarchical self-assembly of graphene-bridged on AgIO₃/BiVO₄: an efficient heterogeneous photocatalyst with enhanced photodegradation of organic pollutant under visible light. *J. Alloy Compd.* 831, 154820. doi:10.1016/j.jallcom.2020.154820

Wang, X., Zhou, C., Yin, L., Zhang, R., and Liu, G. (2019). Iodine-deficient BiOI nanosheets with lowered valence band maximum to enable visible light photocatalytic activity. *ACS Sustain Chem. Eng.* 7, 7900–7907. doi:10.1021/acssuschemeng.9b00548

Xia, Y. M., Zhang, J. H., Xia, M., Zhao, Y., Chu, S. P., and Gao, W. W. (2020). Peony-like magnetic graphene oxide/Fe₃O₄/BiOI nanoflower as a novel photocatalyst for enhanced photocatalytic degradation of Rhodamine B and Methylene blue dyes. *J. Mater Sci. Mater Electron* 31 (3), 1996–2009. doi:10.1007/S10854-019-02719-6

Yang, J., Su, H., Wu, Y., Li, D., Zhang, D., Sun, H., et al. (2021). Facile synthesis of kermesinus BIOI with oxygen vacancy for efficient hydrogen generation. *Chem. Eng. J.* 420, 127607. doi:10.1016/j.cej.2020.127607

Yang, Y., Dai, Y., Hou, J., Jiang, T., Wei, R., Idrees, F., et al. (2019). Ultrathin-layer structure of BiOI microspheres decorated on N-doped biochar with efficient photocatalytic activity. *Front. Chem.* 1, 378. doi:10.3389/fchem.2019.00378

Yang, Y., Zhang, C., Lai, C., Zeng, G., Huang, D., Cheng, M., et al. (2018). BiOX (X = Cl, Br, I) photocatalytic nanomaterials: applications for fuels and environmental management. *Adv. Colloid Interface Sci.* 254, 76–93. doi:10.1016/j.cis.2018.03.004

Yu, Y., Liu, Y., Wu, X., Weng, Z., Hou, Y., and Wu, L. (2015). Enhanced visible light photocatalytic degradation of metoprolol by Ag-Bi₂WO₆-graphene composite. *Sep. Purif. Technol.* 142, 1–7. doi:10.1016/j.seppur.2014.12.025

Yusuf, T. L., Orimolade, B. O., Masekela, D., Mamba, B., and Mabuba, N. (2022). The application of photoelectrocatalysis in the degradation of rhodamine B in aqueous solutions: a review. *RSC Adv.* 12, 26176–26191. doi:10.1039/D2RA04236C

Zhang, F., Peng, H., Jiang, S., Wang, C., Xu, X., and Wang, L. (2019). Construction of precious metal-loaded BiOI semiconductor materials with improved photocatalytic activity for microcystin-LR degradation. *Environ. Sci. Pollut. Res.* 26, 8226–8236. doi:10.1007/s11356-019-04266-3

Zhao, L., Zhang, X., Fan, C., Liang, Z., and Han, P. (2012). First-principles study on the structural, electronic and optical properties of BiOX (X=Cl, Br, I) crystals. *Phys. B* 407, 3364–3370. doi:10.1016/j.physb.2012.04.039

Zhong, S., Wang, B., Zhou, H., Li, C., Peng, X., and Zhang, S. (2019). Fabrication and characterization of Ag/BiOI/GO composites with enhanced photocatalytic activity. *J. Alloy Compd.* 806, 401–409. doi:10.1016/j.jallcom.2019.07.223

Zhou, C., Jiang, C., Wang, R., Chen, J., and Wang, G. (2021). CdS microparticles decorated with Bi⁰/BiOI nanosheets for visible light photocatalytic hydrogen evolution. *ACS Appl. Nano Mater* 4, 4939–4947. doi:10.1021/acsanm.1c00473